



Granting Sensorial Properties to Metal Parts through Friction Stir Processing

Pedro M. Ferreira^{a,*}, Miguel A. Machado^{a,b}, Marta S. Carvalho^{a,b}, Catarina Vidal^{a,b}

^a UNIDEMI, Department of Mechanical and Industrial Engineering, NOVA School of Science and Technology, Universidade Nova de Lisboa, 2829-516 Caparica, Portugal

^b Laboratório Associado de Sistemas Inteligentes, LASI, 4800-058 Guimarães, Portugal

ARTICLE INFO

Keywords:

Self-sensing material
Piezoelectric particles
Solid-state processing technology
Friction Stir Processing
Structural health monitoring

ABSTRACT

Structural Health Monitoring systems assess the part's current condition. This can be performed with a monitoring system comprising sensors, on the surface or embedded, in the monitored parts. However, surface sensors are subject to damage, and embedding the sensors may result in a weakened part. An innovative Self-Sensing Material and its manufacturing process were developed and are presented herein. As proof of concept, Barium Titanate particles were introduced and dispersed into an AA5083-H111 part by Friction Stir Processing (FSP). The particles' distribution and concentration was evaluated by a set of characterization techniques, demonstrating that greater concentrations, grant enhanced sensitivity to the material. The use of FSP and the embedded particles improved the part's mechanical behaviour in the processed zone. The sensorial properties were assessed and the response to a set of dynamic loads was measured, being coherent with the solicitations provided. The developed self-sensing material revealed an electrical sensitivity of $12.0 \times 10^{-4} \mu\text{V}/\text{MPa}$.

1. Introduction

Structural Health Monitoring (SHM) aims to provide an integrity diagnosis of components that constitute a given structure over time. SHM of a component can begin in the design stage, through dimensioning, materials selection, modelling and numerical simulation, RAMS (Reliability, Availability, Maintainability, Safety) analysis, and selection of manufacturing technologies. During the manufacturing stage, component monitoring is also critical. This is guaranteed by quality control mechanisms, destructive characterization, and non-destructive inspection. However, the manufacturing stage extends beyond the manufacturing technology of the component. The component also needs to be monitored during the operation of a production unit, supply chains, logistics network, and transportation, among others. In the in-service stage, the component is inspected, stresses involved are monitored, and in-service damages are calculated using tools available in Fracture Mechanics [1]. Increasingly, experts try to extend the components' life through preventive maintenance actions (before detecting failure), rather than corrective maintenance (after detecting failure). At the end of the component's life cycle it can return to the first stage, where it is redesigned, using data collected in service and during maintenance stage, seeking its optimization in terms of production cost

versus mean lifetime, based on the component's life cycle analysis and its sustainability. Usually, these SHM systems are composed by a set of embedded sensors, sensors network and/or instrumentation. Thus, Sensing Technology (ST) plays a key role in SHM systems, focusing on the development of sensors, sensory systems, or self-sensing materials [2].

Over the last 15 years, ST has shown exponential growth in the technologies developed and their new applications [3,4]. SHM systems can be based on a wide range of embedded sensors or self-sensing materials, such as Fibre-Optic Sensors [5–7] and Piezoelectric Sensors [8–12]. However, other techniques also ensure effective monitoring, such as Capacitive Methods [13] and Electromagnetic Techniques (for example, Eddy Currents [14–16] or Potential Drop measurement [17]), and even materials, such as Shape Memory Alloys [18].

Metallic materials represent most of the structural engineering applications, thus, sensor integration methodologies or self-sensing metal components developments are crucial. Currently, a set of applications allows effective monitoring of metal components without compromising structural integrity. Some of the technologies that allow the sensors' incorporation and produce self-sensing materials are Shape Deposition Manufacturing, Magnetron Sputtering and Electroplating [14,19–23], the Electron Beam Melting [12], Ultrasonic Additive Manufacturing

* Corresponding author.

E-mail address: pdm.ferreira@campus.fct.unl.pt (P.M. Ferreira).

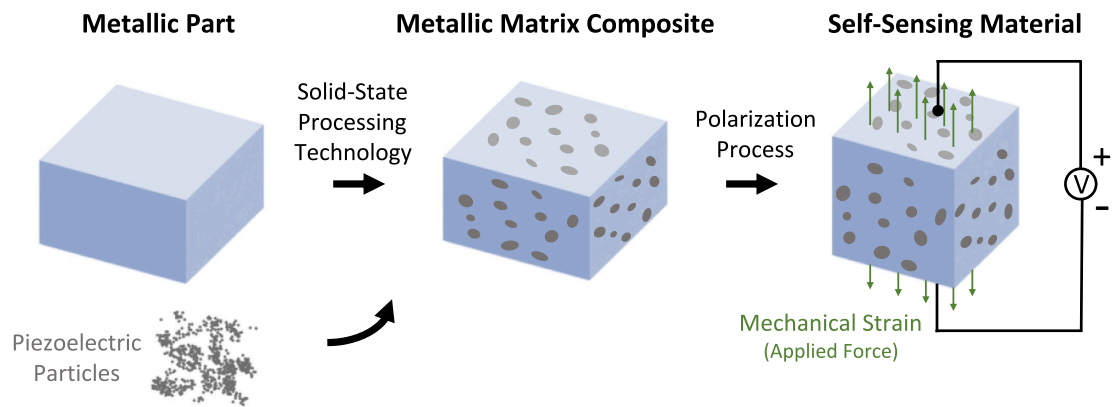


Fig. 1. Schematic representation of the self-sensing material development steps.

[11,24–26], Ultrasonic Metal Welding [27,28], and hybrid manufacturing metal processes with an in-situ process interruption [29]. In these cases, the manufacturing process involves high temperatures which can be a disadvantage.

Solid-state material processing technologies can be an alternative to produce such self-sensing materials, since the temperature involved can remain below 250–300 °C, depending on the material being processed and on the selected process parameters. Instead of blending particles in a melted material, solid-state processing, via Friction Stir Processing (FSP), can be used to introduce and distribute particles, in metallic components, by viscoplastic stirring phenomena. FSP is considered one of the most significant technologies that has been developed in recent decades, due to its energy efficiency, environmental impact, and versatility to process high-strength aluminium alloys (mainly for the aerospace industry) and other metallic alloys, which by conventional fusion processing technologies are difficult or even impossible to process [30,31]. Through FSP, reinforcement materials have been incorporated into metal matrices near the surface, for example, SiC or SiO₃ particles, Al₂O₃ or Al₃Ti or Al₂Cu particles, Ni or NiTi particles, Ti or TiC or TiO₃ particles, Barium Titanate (BT) particles, Lead Zirconate Titanate (PZT) particles, etc. [32–36]. In addition, the use of multi-walled carbon nanotubes improved the wear resistance and hardness of the produced composites when compared to the base alloy, as demonstrated by Akbari et al [37]. Thus, FSP has proven itself to be an effective technological process to incorporate functional particles and, therefore, demonstrates a great potential to produce a self-sensing material [35,38]. In previous studies, surface composites have been obtained by applying a layer of particles in a volatile medium, however nowadays metallic materials surface can be reinforced through particles incorporated by grooves or holes that are previously machined in the component [39]. Furthermore, other methodologies are emerging, such as Upward Friction Stir Processing (UFSP) [40].

The piezoelectric effect is an interesting phenomenon that is inherent to a set of materials. These materials are widely used in some ST applications and non-destructive testing through ultrasound testing. Piezoelectric ceramics of PZT type, in their various applications, are the predominant ceramics used. In addition, other materials such as PT (PbTiO₃), PMN (Pb (Mg_{1/3} Nb_{2/3}) O₃) and BT (BaTiO₃), are used in devices that require special and very specific properties, such as high-temperature transducers [41–43]. The inclusion of piezoelectric materials into metal matrices by FSP has shown to improve the mechanical and damping properties and/or to modify electrical properties of the base material [43,44]. Consequently, piezoelectric materials represent an opportunity for the development of self-monitored materials.

In this work, a new self-sensing material is proposed and validated. Determining the component's current state will decrease costs associated with planned maintenance interventions and guarantee the health and safety of the component and its surroundings, with appreciable

social, economic, and environmental impacts. So, a metallic plate with embedded piezoelectric particles by FSP was manufactured and underwent a polarization process generating a self-sensing material. The developed self-sensing material was characterized in terms of particles distribution, mechanical behaviour and sensitivity to dynamic loads.

2. Process Innovation: Self-Sensing Material

Structural engineering applications require effective and reliable. This can be ensured by SHM through a network of embedded or surface sensors. However, these can be damaged during the incorporation process or throughout the part's life cycle. Aiming to counteract these problems, a technology was developed which confers regions with sensorial properties to metal parts, avoiding coupling sensors, i.e., a self-sensing material. The implementation of this material aims to provide metal components self-sensing ability in real-time and throughout their life cycle, without compromising their structural integrity.

This self-sensing material key element are piezoelectric particles evenly incorporated in a metal part. The piezoelectric particles were used for their piezoelectric effect, they can generate an electrical signal when subjected to mechanical strain. To embed the piezoelectric particles into the metal part, a solid-state processing technology was used since it allows an evenly particles distribution over the processed region, low processing temperatures (compared to metal melting processes) and improved mechanical strength by strain hardening. Since this is a chaotic process, the particles will be randomly distributed which will result in random particles orientation. Thus, a polarization process must be carried out, to reorient the electrical dipoles of the piezoelectric particles which will grant the desired sensorial properties. A schematic of the self-sensing material concept development steps is depicted in Fig. 1.

This self-sensing material technology can be used to produce a value-added product, i.e., a structural component with an embedded monitoring system that allows its monitorization from manufacturing to the end of its life cycle. Thus, this self-sensing material may pave the way for the development of research in areas of reliability, maintenance, and maintenance management. As proof of concept, a self-sensing material based on Barium Titanate (BT) piezoelectric particles embedded into an AA5083-H111 plate by Friction Stir Processing (FSP) was manufactured followed by a polarization process. To evaluate its sensing properties, a set of laboratory tests were conducted. The material was subjected to dynamic solicitations to evaluate its sensing properties. In addition, some tests were also performed to provide a structural and mechanical characterization of the self-sensing material developed.

Table 1
AA5083-H111 chemical composition (wt%) [45].

	Si	Fe	Cu	Mn	Mg	Cr	Zn	Ti + Zr	Al
Min				0.4	4	0.05			
Max	0.4	0.4	0.1	1	4.9	0.025	0.25	0.15	Remaining

Table 2
Piezoelectric and mechanical properties of AA5083-H111 [46,47].

Piezoelectric and Mechanical Properties	AA5083-H111
Dielectric Constant (K_{33})	[54.906, 54.789]
Piezoelectric Constant (d_{33}) [pC/N]	$[-1.0, -1.7]10^{-8}$
Electrical Conductivity [%IACS]	27.9
Vickers Hardness [HV]	91
Modulus of Elasticity [GPa]	71.0
Yield Strength [MPa]	213

3. Materials and Methods

3.1. Materials

The self-sensing material was produced using commercial AA5083-H111 plates with dimensions of 203 (rolling direction) \times 103 \times 10 mm as base material. The nominal chemical composition of the AA5083-H111 is presented in Table 1 [45]. The piezoelectric and mechanical properties are listed in Table 2 [46]. Dielectric and piezoelectric constants are some of the most important piezoelectric properties of materials, so, when the applied force is parallel to the dipole, there is an enhancement of the spontaneous polarization. This is called the d_{33} and k_{33} effect. When force is applied perpendicular to the dipole moment, it develops a transverse electric charge, and this is called the d_{31} and k_{31} effect.

Commercial BT particles (BaTiO_3), with 99,5% of purity, were used as functional and reinforcement particles. The particles size is smaller than 2 μm . The morphology and size of the BT particles are illustrated in Fig. 2. Fig. 2 a depicts the BT particles homogeneous granular morphology and Fig. 2 b the presence of Oxygen (O), Titanium (Ti) and Barium (Ba) confirmed by energy-dispersive X-ray spectroscopy (EDS) analysis. For this analysis a scanning electron microscope (SEM) ZEISS DSM 962 was used. The particles' conductivity was improved with a thin coating of conductive gold (Polaron E-5100). The piezoelectric and mechanical properties are listed in Table 3.

BT particles are piezoelectric ceramics with numerous microscopic ferroelectric crystals. These small crystals have a Perovskite crystalline structure, which has tetragonal, rhombohedral, or simple cubic symmetry, depending on the temperature [49]. When the ceramic is below a

Table 3
Piezoelectric and mechanical properties of BaTiO_3 [48].

Piezoelectric and Mechanical Properties	BaTiO_3
Dielectric Constant (K_{33})	1700
Piezoelectric Constant (d_{33}, d_{31}) [pC/N]	190, -78
Electromechanical Coupling Coefficient (k_{33}, k_{31})	0.50, 0.21
Curie Temperature (T_c) [$^\circ\text{C}$]	115
Density [g/cm^3]	6.08

certain critical temperature, known as Curie temperature, the Perovskite structure presents tetragonal symmetry, and consequently an electric dipole. However, when the ceramic is above the Curie temperature, the crystalline structure changes, becoming rhombohedral or simple cubic without an electric dipole [50]. The existence of this dipole causes the crystalline structure to deform in the presence of an electric field or generates an electrical displacement when subjected to mechanical strain. The mechanical strain or variation of the electric dipole does not necessarily imply macroscopic effects, because the dipoles form arrangements in domains, which in turn are randomly distributed in the polycrystalline material [51]. For macroscopic manifestations, a preferential orientation is needed in these domains, known as polarization. Even this polarization fades with use and time, causing the material to no longer transform electrical energy into mechanical energy, or vice versa [42,43].

3.2. Self-Sensing Material Fabrication

The self-sensing material was fabricated by incorporation of BT particles within the AA5083-H11 plate via FSP. The groove method was selected to place the particles since it allows greater control of the amount deposited in the plate when compared to holes method [39] or UFSP [40].

To evaluate the effect of groove dimensions, and to optimize particles distribution and concentration, four distinct plates were produced, as described in Table 4. The grooves were machined by milling. Following this step, the piezoelectric particles were deposited and compacted in the plates' groove. An additional plate was prepared without a groove or particles, to be used as a reference (plate #5).

FSP was performed with a set of tools depicted in Fig. 3: a) the first

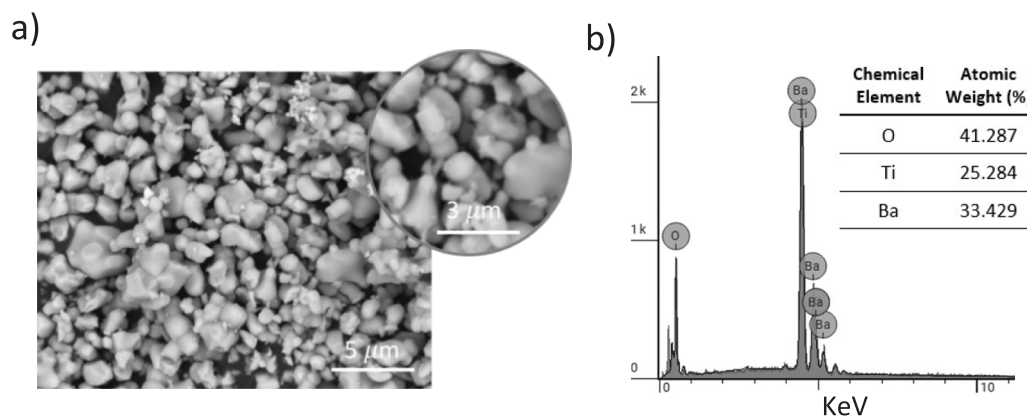
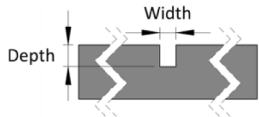


Fig. 2. Physicochemical characterization of Barium Titanate particles (BaTiO_3): a) scanning electron microscopy image; b) chemical elemental mapping determined by energy-dispersive X-ray spectroscopy.

Table 4
Groove dimensions produced to evaluate particles distribution and concentration.

Plate #.	Groove Dimensions [mm]		Cross Section Area (A_s) [mm ²]	Amount of Embedded Particles [g]	Schematic Representation
	Depth	Width			
1	2	3	6	7.30	
2	4	3	12	14.60	
3	3	2	6	7.30	
4	3	4	12	14.60	
5	No groove. For reference only.				

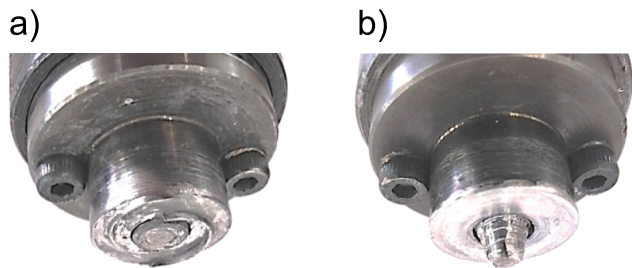


Fig. 3. FSP tools used: a) pinless FSP tool used to close the groove trapping the particle; b) pinned FSP tool to disperse the particles within the metal.

tool was composed of a left-hand scrolled shoulder without pin (pinless FSP tool), and b) the second was composed of a featureless concave shoulder and a triflute left-handed conical pin (pinned FSP tool). The selection of this pinned FSP tool was based on research developed by Inácio *et al.* [40] and Vidal *et al.* [33], which demonstrated that this pinned FSP tool geometry ensures a good particle distribution. The shoulder of both tools had a diameter of 19 mm. A 14° conical pin with a bottom diameter of 5 mm was used. All tools were made of H13 steel. The tools rotated clockwise with a rotation speed (ω) of 1120 rev/min and travelling speed (v) of 112 mm/min. The tools were tilted by 1°, to help the forging action at the travelling edge of the shoulder. The

parameters used in this process were based on a study developed by Bajakke *et al.* [35], to ensure the best particles distribution.

To embed the BT particles into the plates, three steps were performed as depicted in Fig. 4. First, BT particles were compacted into a single machined groove, as shown in Fig. 4. Then, a pass was performed with the pinless FSP tool, to close the groove and confining the particles inside. Finally, using the pinned FSP tool, four passes were performed, in the same direction (Y) and without offset in the X direction, to ensure a greater distribution and homogeneity of the particles along with the nugget as recommended by Bajakke *et al.* [35]. The plate #5 (reference plate) was only subjected to the third step, i.e., the four passes with the pinned FSP tool.

FSP causes BT particles random distribution inside the plate, therefore for macroscopic electrical effect was needed to impose a preferential orientation of the randomly distributed electrical dipoles' arrangements of the BT particles. Thus, a polarization process was carried out applying a strong electrical field (9 kV/mm) in a controlled environment at 90 °C, to create an asymmetry in the previously unorganized compound. The strong electrical field causes a reorientation of the spontaneous polarization. At the same time, domains with a favourable orientation to the polarity field direction grow and those with an unfavourable orientation shrink. The domain walls are shifted in the crystal lattice. After polarization, most of the reorientations are preserved even without the application of an electrical field. However, a small number of the domain walls are shifted back to their original position, e.g., due to internal mechanical stresses. The schematic

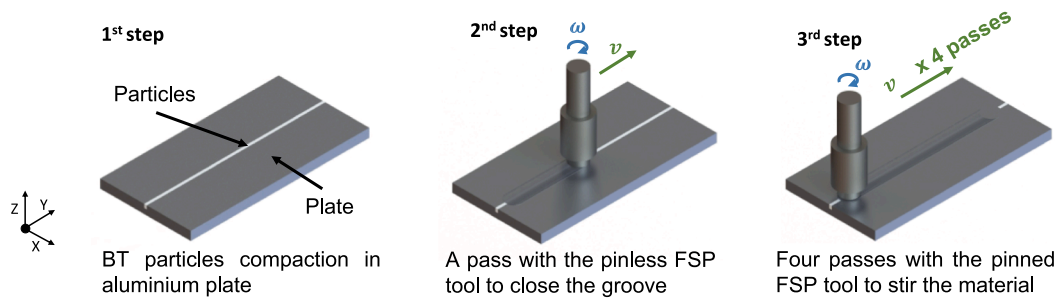


Fig. 4. Steps performed to embed the particles in the metal.

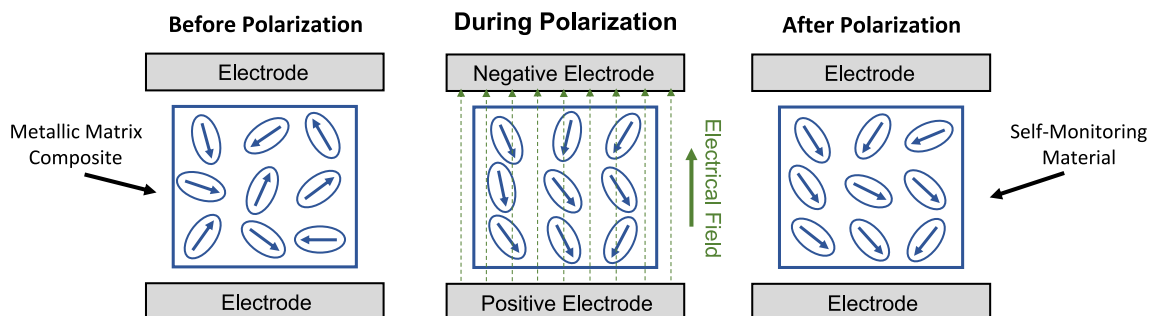


Fig. 5. Schematic of the polarization process.

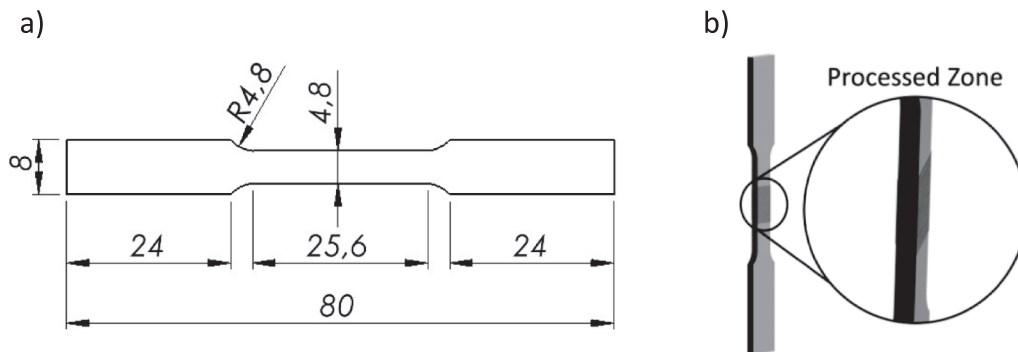


Fig. 6. Uniaxial tensile test sample: a) schematic drawing with dimensions in mm; b) processed zone closeup.

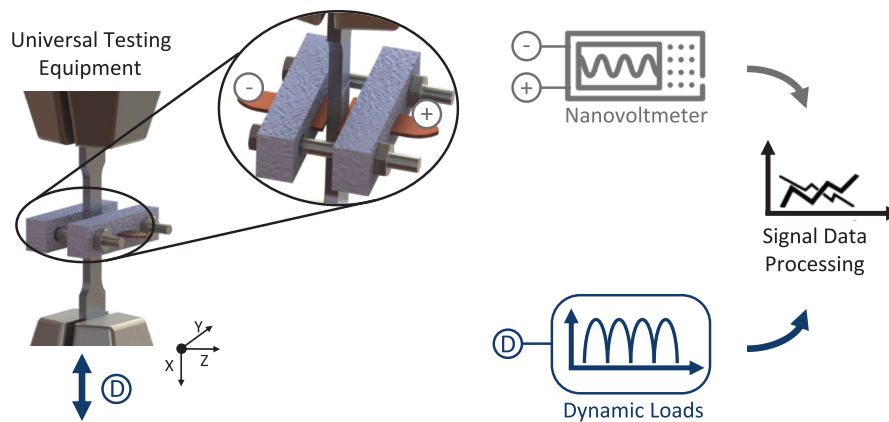


Fig. 7. Experimental setup used to analyse the dynamic response of the self-sensing material.

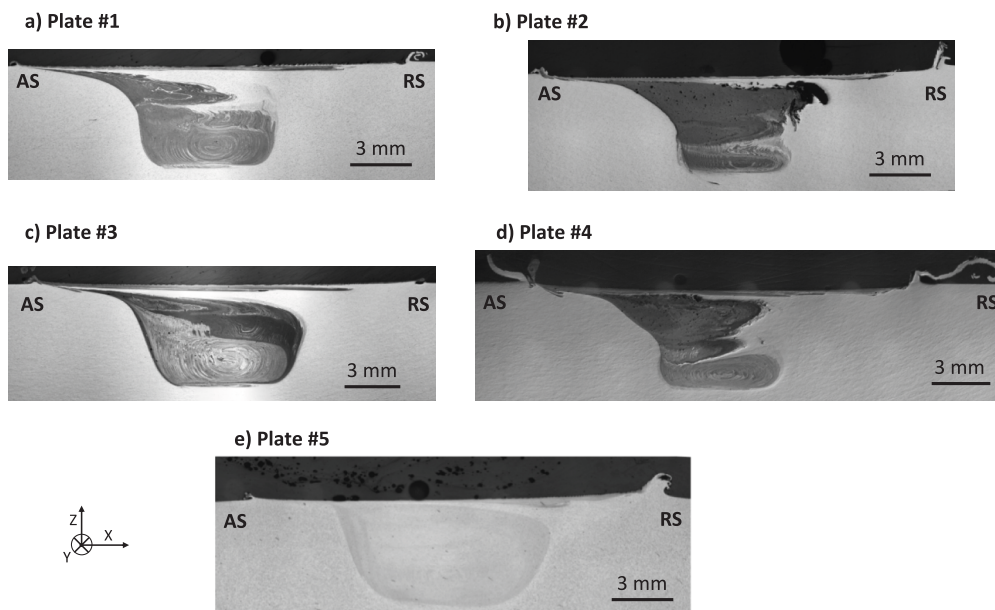


Fig. 8. Macrostructure of the self-sensing materials: a) plate #1, b) plate #2, c) plate #3, d) plate #4, e) plate #5.

diagram of the polarization process is depicted in Fig. 5.

The polarization of piezoelectric particles can be very challenging when embedded in metals since the polarization consists of in the application of high electrical fields in the processed region. However, inside metals, the electric field is almost nil, under the right conditions, this polarization process is possible.

3.3. Self-Sensing Material Characterization

The particle's distribution and concentration inside the self-sensing material was analysed using macrostructural and physicochemical characterization techniques. In addition, the mechanical behaviour and the electrical conductivity of the self-sensing material was evaluated

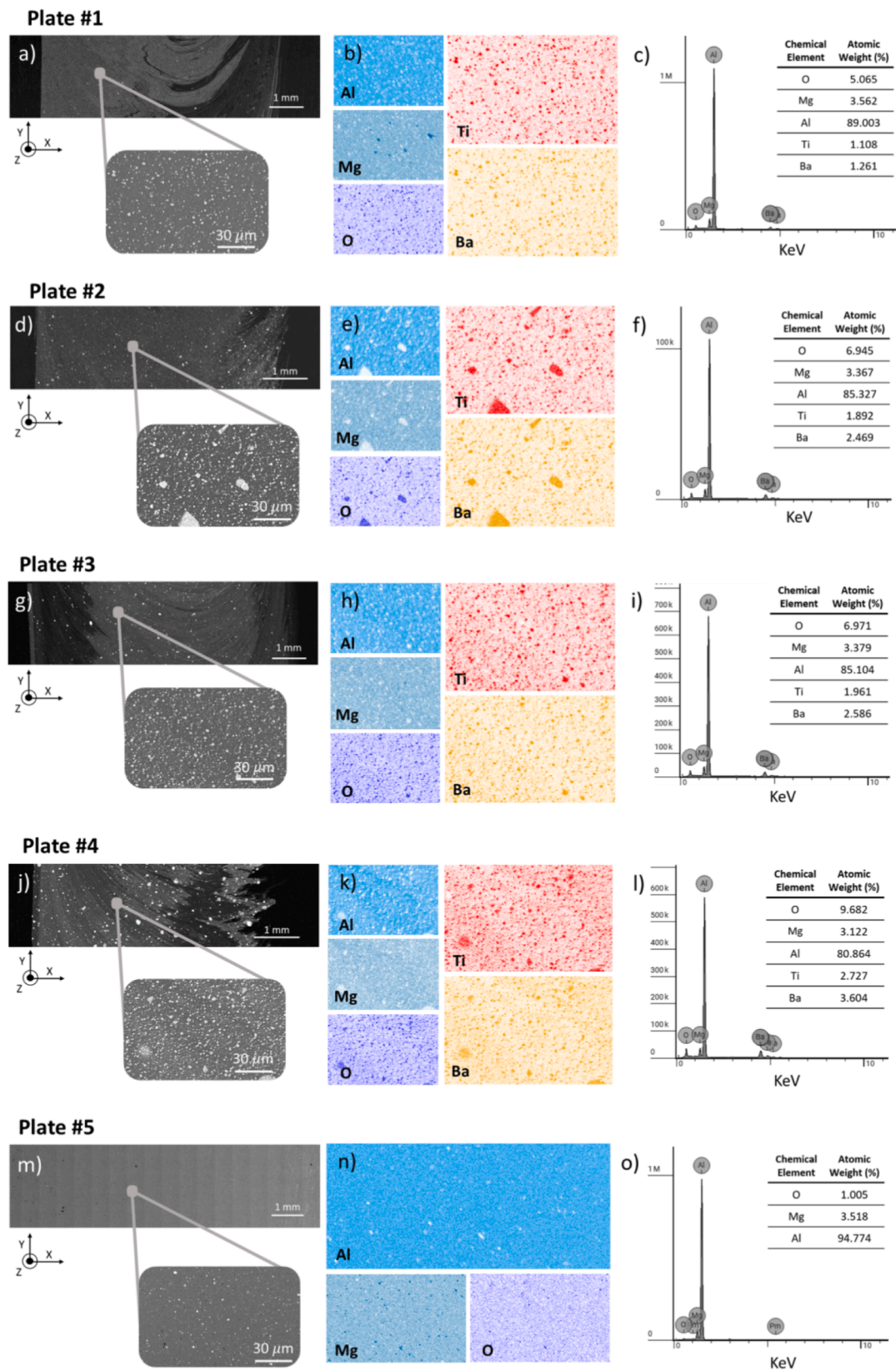


Fig. 9. Physicochemical characterization of the plate #1 (a – c), #2 (d – f), #3 (g – i), #4 (j – l) and #5 (m – o): scanning electron microscopy (SEM) images (a, d, g, j, m); chemical elemental mapping determined by energy-dispersive X-ray spectroscopy (EDS) (b, e, h, k, n); chemical elemental composition determined by EDS (c, f, i, l, o).

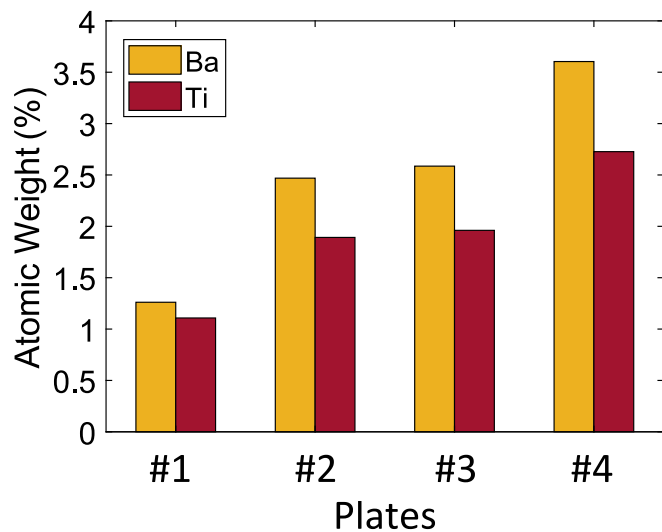


Fig. 10. Atomic weight of the BT particles within the plates.

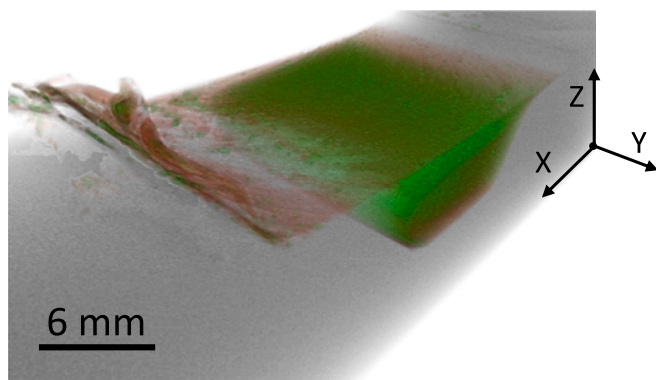


Fig. 11. 3D representation of plate #4 obtained by μ -CT analysis: particles distribution (green colour); nugget (red colour); aluminium alloy (grey colour). (For interpretation of the references to colour in this figure legend, the reader is referred to the web version of this article.)

using others characterization techniques, such as, uniaxial tensile tests, microhardness measurements and electrical conductivity measurements.

3.3.1. Macrostructural Characterization

Macrostructural analyses of the self-sensing material and the processed plate #5 were performed using an Olympus CX40 optical microscope and a 2x magnification lens, to reveal the macrostructure and particles distribution. All samples, specifically prepared for this analysis, were fitted in epoxy resin, grounded and polished following standard metallographic procedures, and then etched in Kelle's reagent. Regarding the self-sensing materials, the main macrostructural regions, namely the nugget, where the BT particles were in-bluid, were identified and characterized.

3.3.2. Physicochemical Characterization

A more detailed characterization of the samples was achieved by using scanning electron microscopy (SEM) with a ZEISS DSM 962 apparatus and the elemental chemical composition was assessed by the corresponding X-ray energy dispersive spectrometer (EDS). Whenever required, the conductivity of the BT particles was improved with a thin coating of conductive gold (Polaron E-5100). The 3D micro-architectural morphology of plate #4 was characterized by X-Ray microtomography (μ CT), using a Phoenix V|TOME|X, GE, according to

the procedure conducted by Vidal *et al.* [33]. The acquired image data were interpreted qualitatively and quantitatively using 3D tomographic reconstruction and analysis software (Volume Graphics 3.04 software).

3.3.3. Uniaxial Tensile Tests

Uniaxial tensile tests were performed at room temperature using a servo-hydraulic MTS 312.21 testing machine with a load capacity of 100 kN, according to the ASTM E8/E8M-13a standard. For this purpose, uniaxial tensile test specimens were produced using a HAAS Super Mini Mill 2 CNC Machining Center, according to the geometry presented in Fig. 6 a. All specimens were prepared with a thickness (t) of 2 mm, ensuring accessibility to both sides of the nugget (Fig. 6 b). The uniaxial tensile tests were used to characterize the mechanical behaviour of the self-sensing material.

3.3.4. Microhardness Measurements

A Mitutoyo HM-112 microhardness testing machine was used to perform the Vickers microhardness profile along the length (X direction) of the samples specifically prepared for this analysis, according to the ASTM E384 – 10 standards. For this purpose, the samples top surface was milled down 1 mm, grounded, and polished to obtain a homogenous surface condition. The spacing between consecutive indentions was 1 mm for the base material and 0.5 mm for processed and thermal/mechanical affected regions. The load used was 0.5 kgf applied for 10 s. These microhardness measurements were performed to characterize processed and non-processed zones, and to evaluate the particles' distribution.

3.3.5. Electrical Conductivity Measurements

Eddy currents and potential drop measurement techniques were used to characterize the electrical conductivity of the samples described in the section 3.3.4, according to the procedure developed by Sorger *et al.* [52] and Santos *et al.* [53]. The electrical conductivity was measured along a straight line along the X direction. For the eddy currents technique, a pencil probe operating at 2 MHz (corresponding to a penetration depth of 0.019 mm for this alloy) was used with a NORTEC 600 D impedance analyser. The potential drop measurements were performed with a four-point probe with four straight aligned tungsten needles with a radius of 0.4 μ m. A current of 80 mA was imposed to the external needles with a Keithley SourceMeter 2450. A Keithley Nanovoltmeter 2182A was used to measure the voltage between the two inner needles allowing the calculation of the electrical conductivity.

3.4. Sensorial Properties Assessment

The potential self-sensing ability of the material comes from the presence of the piezoelectric particles inside. Thus, to prove that the sensing properties are granted to the metal part, a set of laboratory tests was performed. These tests intended to evaluate the part's electrical response when subjected to dynamic solicitations.

To assess the self-sensing material response to dynamic solicitations an MTS 312.21 was used to apply dynamic loads. The specimens used for this analysis were uniaxial tensile test specimens obtained through the same manufacturing process and with the same size than those in Fig. 6. Each uniaxial tensile test specimen was subjected to dynamic loads. The dynamic load spectrum was characterized by fifteen tensile cycles with a frequency of 0.25 Hz. To analyse the sensitivity of the uniaxial tensile test specimens five different dynamic load intensity values were applied. The load intensity was set by displacement (X direction) control with amplitudes of 0.02, 0.03, 0.04, 0.05 and 0.1 mm, respectively.

Regarding the acquisition system, a load cell was used to measure the force induced by the dynamic loads. To monitor the electrical voltage response an electrical link connected to the sample was used which allowed direct contact with the sample surface, has shown in Fig. 7. The electrical response was monitored by a Keithley Nanovoltmeter 2182A connected to a National Instruments DAQ and assisted by a LabView

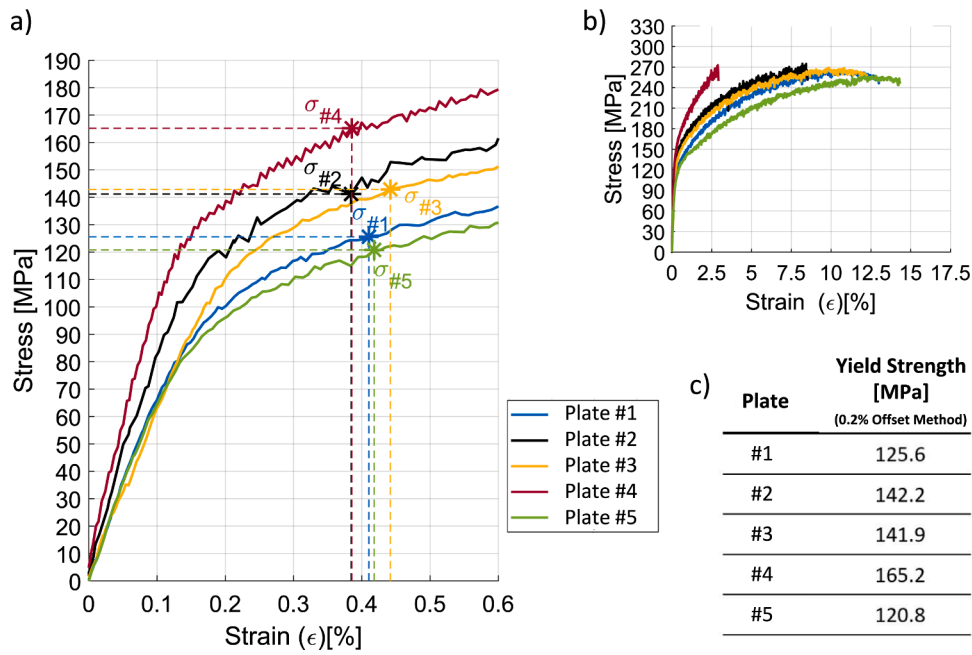


Fig. 12. Uniaxial tensile test results: a) elastic region, b) tensile stress–strain curves, c) yield strength.

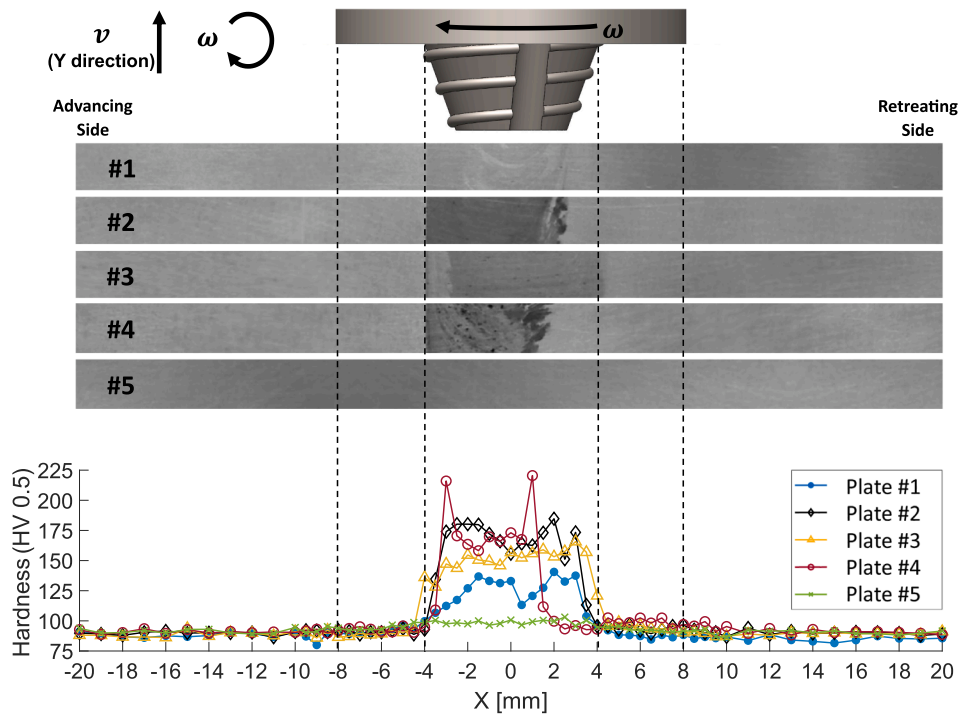


Fig. 13. Microhardness profile along the X direction of the plates.

program for signal data processing. All testing were carried out at room temperature.

4. Result and Discussion

4.1. Self-Sensing Material Characterization

4.1.1. Macrostructural and Physicochemical Characterization

Macrostructural characterization allowed the analysis of the particles' distribution in the processed zone and the influence of using

different groove dimensions to incorporate the particles in the plates. Fig. 8 presents the macrostructure of the samples. The plates #1 and #3 (Fig. 8 a, c) were manufactured using a groove sectional area smaller than that of the plates #2 and #4 (Fig. 8 b, d). So, from Fig. 8, it is possible to observe that plates #1 and #3 present, in the processed zone, a particles' distribution less dense than that of plates #2 and #4. Indicating that, plates #1 and #3 present less particles than plates #2 and #4. Such was expected, due to the difference between the groove sectional area of the plates.

When comparing plates with the same groove sectional area, i.e,

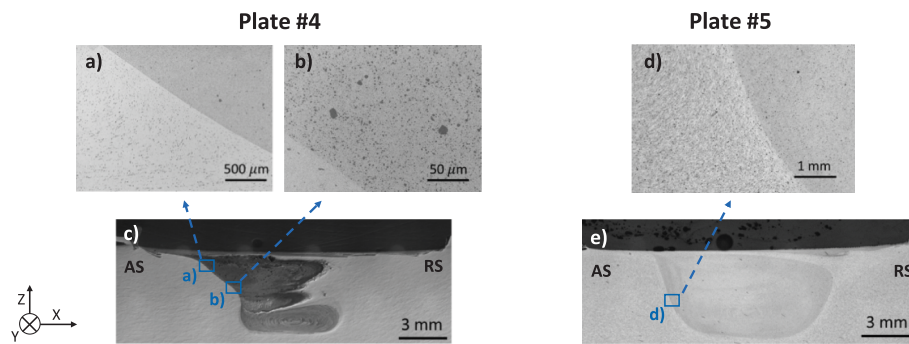


Fig. 14. Metallographic results: plate #4 (a – c) and plate #5 (d, e).

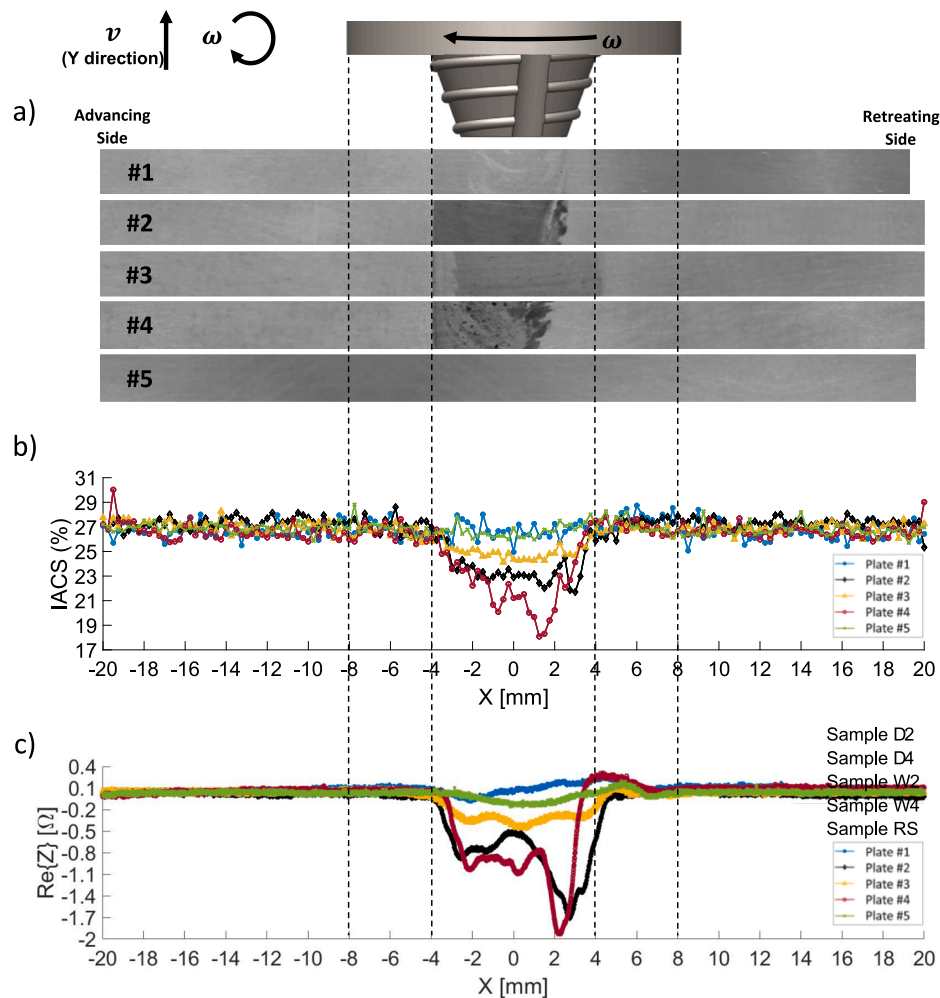


Fig. 15. Electrical conductivity profile: a) macrography; b) electrical conductivity obtained from the linear four-point probe; c) impedance change obtained from the Eddy currents technique.

plate #1 with #3, and #2 with #4, the results obtained show a sharper distribution in plates #3 and #4. So, for each case, their groove geometry led to an improved particle distribution and concentration in the processed zone.

Fig. 8 e shows the stir zone of the plate #5 and the thermal/mechanical affected region of friction stir processed material.

The presence of Oxygen (O), Manganese (Mg), Aluminium (Al), Titanium (Ti), Barium (Ba) on the self-sensing material was confirmed by EDS analysis. In Fig. 9, the physicochemical characterization of plates #1, #2, #3, #4 and #5 is depicted, i.e., the SEM images. The chemical

elemental mapping and composition determined by EDS was used to characterize the physicochemical properties. Note that the SEM images were acquired in regions with uniform distribution of the BT particles. In contrast, the plate #5 only presents the AA5083-H111 chemical elements, which it is possible to observe in Fig. 9 (m-o).

The results presented in Fig. 9 are summarised in Fig. 10, where it is possible to find the atomic weight of the BT particles within different processed plates. The plate with the highest BT atomic weight was plate #4, presenting a region with an atomic weight of 3.604% of Ba and 2.727% of Ti. The plate with the lowest atomic weight was plate #1,

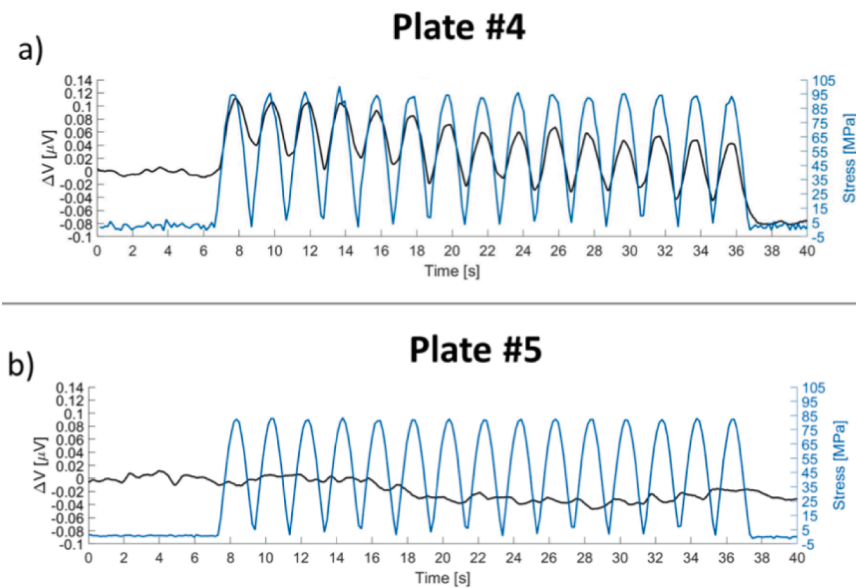


Fig. 16. The influence of the BT particles incorporation in structural metal components when applying a stress intensity of ≈ 100 MPa: a) Plate #4 and b) Plate #5 show a change in the electrical voltage measured in agreement with the stress loads applied.

with an atomic weight of 1.261% for Ba and 1.108% for Ti. Regarding plates #2 and #3, they present practically the same atomic weight. Fig. 11 shows the 3D μ -CT images of plate #4. The particle distribution (green colour) can be seen inside the nugget (red colour). From Fig. 11, one can see that the particles were uniformly and spatially distributed along the processed zone. Furthermore, it is possible to see that the processed zone lacked internal porosities.

Comparing plates with the same groove sectional area (plate #1 with #3, and #2 with #4), the atomic weight has increased. This is explained due to an improved particles distribution and concentration in the processed zone of the plates #3 and #4.

4.1.2. Uniaxial Tensile Tests

Uniaxial tensile tests were used to characterize the mechanical behaviour of the self-sensing material (plates #1, #2, #3 and #4) and the processed reference plate (plate #5). Fig. 12 a - b depict the stress/strain curves where it is possible to note that the presence of the BT particles in the aluminium plates increased their yield strength, when compared to plate #5. Furthermore, the particles incorporation in the aluminium matrix increases the plates' brittleness (Fig. 12 b). This behaviour was in line with the macrostructural and physicochemical characterization results, i.e., with the increase of the BT atomic weight, the yield strength, obtained using the 0.2% offset method, increased as shown in Fig. 12 c, and more brittle the plates became.

4.1.3. Microhardness Measurements

Microhardness can be an indicator of the processing conditions in terms of mechanical strength since it is directly proportional to it [54]. Fig. 13 depicts microhardness profiles for each plate (#1, #2, #3, #4 and #5). In Fig. 13, it is also possible to identify the advancing and retreating side location. A significant increase in hardness can be observed in the stirred zone for plates with build-in particles when compared to plate #5.

The plate with maximum hardness was plate #4, presenting a region with a hardness of ≈ 200 HV0.5. The plate with lowest hardness was plate #1, with a hardness of ≈ 125 HV0.5. It should be noted that this hardness increase occurs in the stirred zone because this is where the BT particles are found. The plates #1, #2 and #3 present a uniform hardness in the stirred zone and higher values than in non-processed zones. Regarding plate #4, it features two peaks of hardness in the stirred zone, and also higher values than non-processed zones. These peaks are

located at the nugget boundaries.

The hardness increase in the plates' stirred zone is caused by, at least, two phenomena, grain refinement due to the dynamic recrystallization (Fig. 14 d, e) and the presence of piezoelectric particles in the nugget (Fig. 14 a - c). Plate #5 shows that the hardness increase comes mainly from the particle's presence and not from grain size reduction.

4.1.4. Electrical Conductivity Measurements

Eddy currents testing and potential drop measurements are expedited techniques to assess microstructural changes in thermomechanical processed materials, which complements the hardness measurements [54,55]. Other works have shown that electrical conductivity is inversely proportional to hardness and consequently to mechanical strength [52,53]. As such, refined zones have lower electrical conductivity, since additional grain boundaries reduce the electronic mobility, while the thermal affected zones have higher electrical conductivity due to the grain growth [52,53]. Fig. 15 depicts the electrical conductivity profiles for each plate. To characterize the electrical conductivity, eddy currents testing (Fig. 15 c) and potential drop measurements (Fig. 15 b) were performed, the results are in good agreement with the microhardness profiles presented in Section 3.3.4. The results show that the plates electrical conductivity of is inversely proportional to microhardness and consequently to mechanical strength. BT particles have significantly affected the electrical conductivity, it is possible to observe an electrical conductivity reduction in the nugget region of plates #2, #3 and #4. Regarding plate #1, which corresponds to sample with lowest atomic weight of BT particles, the electrical conductivity is slightly affected. The asymmetric electrical conductivity profiles were caused by the FSP asymmetry that promotes higher particles concentration on the retreating side, which is demonstrated in the macrostructural characterization. The incorporation of the BT particles leads to a reduction in electrical conductivity of about 10% IACS, i.e., for values of $\approx 18\%$ IACS from the base 27% IACS.

4.1.5. Summary of the Results

The characterization results suggested that there are mechanical properties improvements with the incorporation of the BT ceramic particles. The self-sensing material presented a higher yield strength and hardness than the processed material without BT particles. However, the processed self-sensing material presents an increased brittleness. The distribution and concentration of the BT particles in the self-sensing

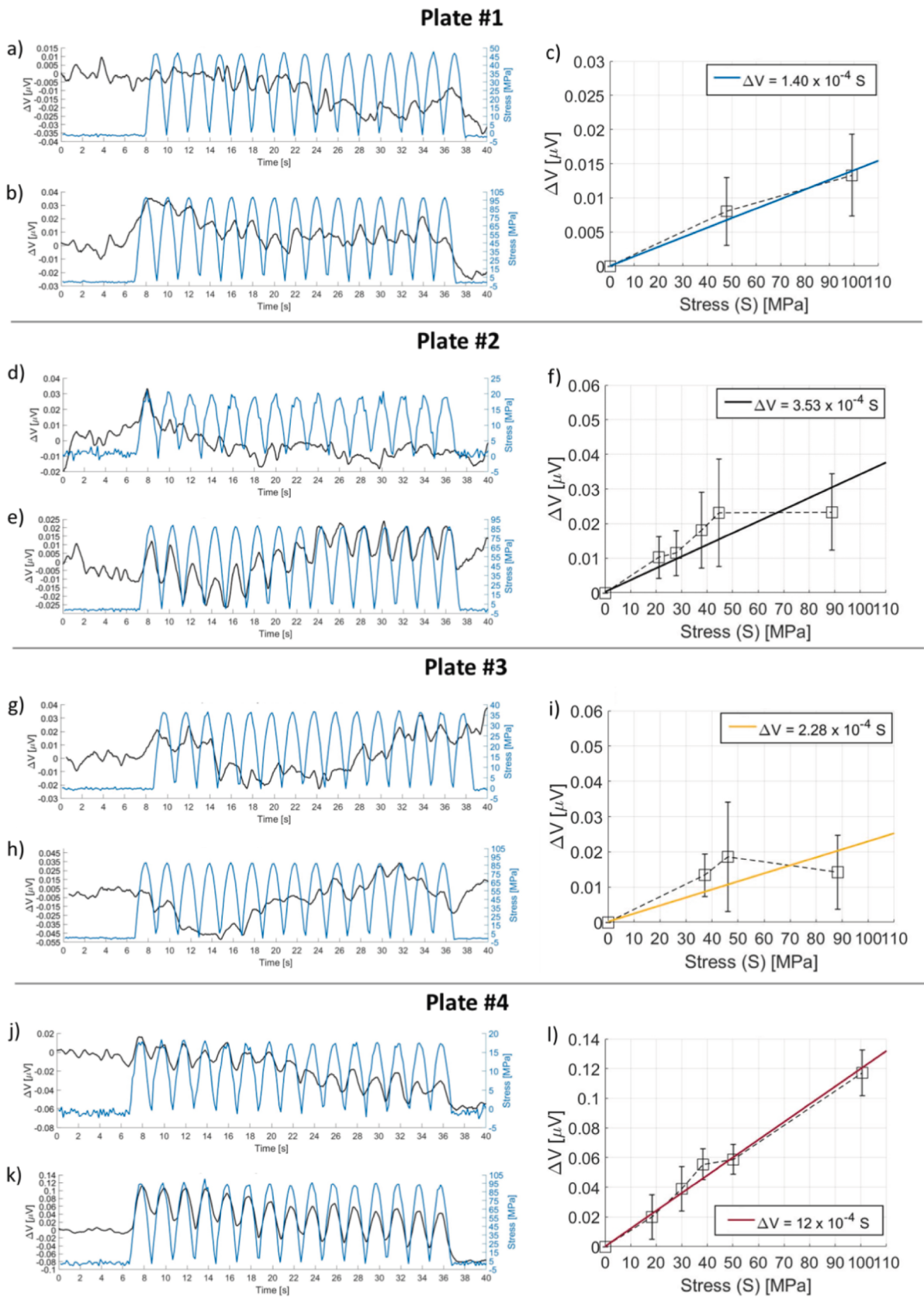


Fig. 17. Response to dynamic loads of plate #1 (a – c), #2 (d – f), #3 (g – i), #4 (j – l): a) response of the lower intensity loading represented in c), b) response of the greater intensity loading represented in c), d) response of the lower intensity loading represented in f), e) response of the greater intensity loading represented in f), g) response of the lower intensity loading represented in i), h) response of the greater intensity loading represented in i), j) response of the lower intensity loading represented in l), k) response of the greater intensity loading represented in l), m) response of the greater intensity loading.

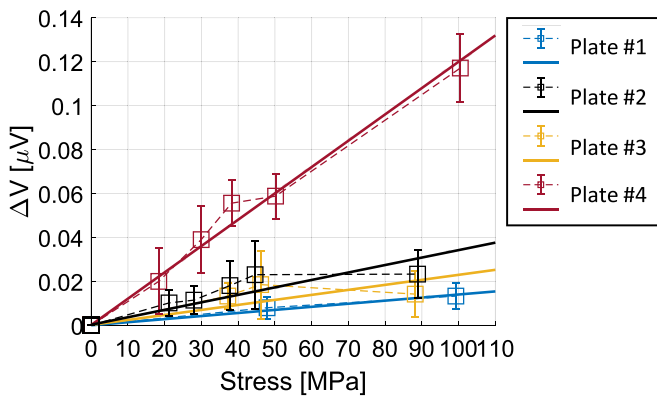


Fig. 18. Response to dynamic loads.

material clearly affects its mechanical behaviour. Finally, the characterization techniques used present matching results with plate #4 presenting the greatest mechanical performance.

4.2. Sensorial Properties Assessment

The sensorial properties were assessed by applying dynamic loads and monitoring the electrical response of the self-sensing material. In Fig. 16 shows plate #4 and plate #5 responses when applying a dynamic load (displacement amplitude of 0.1 mm). This result allowed to verify that the absence of the BT particles in the aluminium matrix does not conduct to an unequivocal electrical response, presenting only noise. In contrast, the self-sensing material presented an evident response in phase with the dynamic loads.

To analyse the influence of different BT particles concentrations, a set of dynamic loads was applied on plates #1, #2, #3 and #4. In Fig. 17, it is possible to observe the self-sensing materials' response to dynamic loads, as well as the stress amplitude. It is worth highlighting that the load amplitude throughout the tests led to uniaxial stresses below the yield strength, i.e., all the tests were conducted in the linear elastic region to satisfy the service conditions to which components are subjected during life cycle. According to the results presented in Fig. 17 c, f, i, l, the highest load applied led to a tensile stress of ≈ 100 MPa.

The electrical response measured during the dynamic loading of

plate #1 (Fig. 17 a, b, c) was verified for a stress above 50 MPa with voltage variation (ΔV) of $\approx 0.008 \mu V$. Plate #1 revealed a sensitivity of $1.40 \times 10^{-4} \mu V/MPa$. Regarding plate #2, the electrical response presented a clear signal for a stress of ≈ 100 MPa, which can be observed in Fig. 17 e. Fig. 17 d depicts the response for lower amplitudes, so this signal presents a synchronous trend with the dynamic loads. The sensitivity of plate #2 is $3.53 \times 10^{-4} \mu V/MPa$, higher than that of plate #1, due to the highest atomic weight of the BT particles.

Plate #3 presented a sensitivity for stresses above to ≈ 35 MPa. According to the experimental results (Fig. 17 i), plate #3 presented a sensitivity of $2.28 \times 10^{-4} \mu V/MPa$. As far as plate #4, the results shown in Fig. 17 l were very promising, because the sample revealed an excellent electrical response to the dynamic load, i.e., all loads applied to plate #4 conducted to a clear and synchronous response. A sensitivity of $12.0 \times 10^{-4} \mu V/MPa$ was recorded, and this result is the highest of all experimental tests.

In brief, Fig. 18 presents experimental results compilation, where it is possible to compare the sensitivity of all samples produced with different BT particles' atomic concentrations. By the analysis of these results, it is perceptible that plate #4, with 3.604/2.727% of BT particles atomic concentration, turned out to be the self-sensing material with the best electrical response for all loading amplitudes and the highest mechanical properties, as shown in Section 4.1.5.

The electrical responses obtained were in good agreement with all previous characterizations, so the BT particles incorporated inside the aluminium matrix granted an electrical response to the self-sensing material when it was subject to dynamic loads. In addition, the BT particles' amount embedded was proportional to the electrical response of the self-sensing material.

4.3. The Influence of the Polarization Process

The plate #4, with the highest sensitivity, was used to evaluate the importance of the polarization process. Being the self-sensing material matrix metallic, it was expected that the polarization process would cause little impact on the reorientation of the electrical dipoles. However, the incorporation of the ceramic particles and the grain refinement caused by the FSP helped the polarization process because the region electrical conductivity decreased. This electrical conductivity reduction is important because with the electron's mobility decreases, and the polarization process becomes more effective. Fig. 19 a depicts the

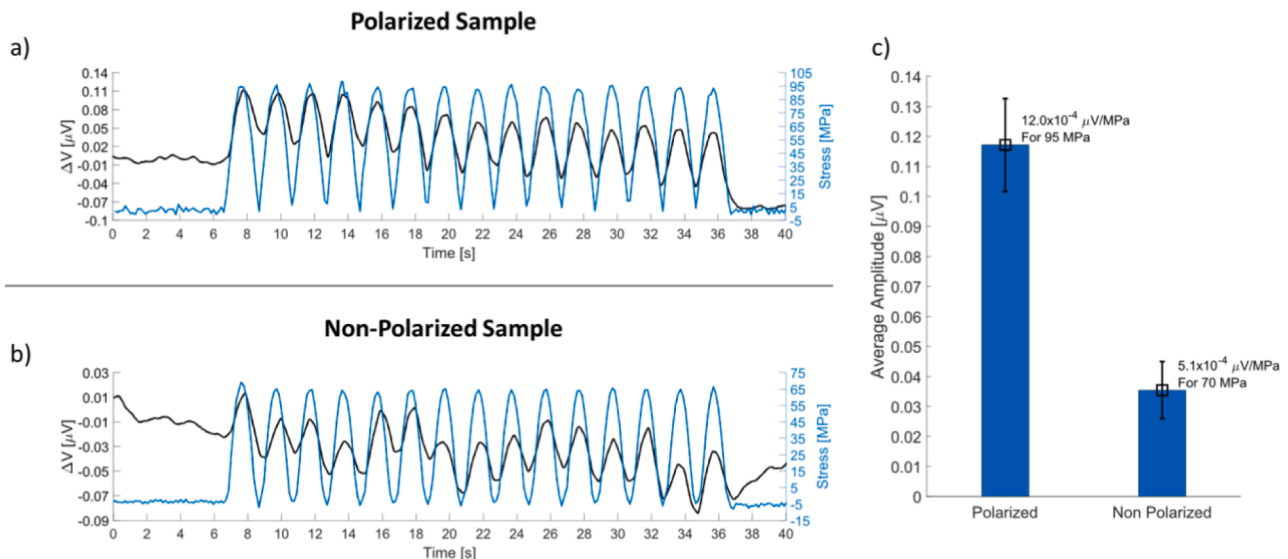


Fig. 19. The influence of the polarization process: a) response of the plate #4 polarized, b) response of the plate #4 non-polarized, c) sensitivity of the polarized and non-polarized samples.

response of the polarized sample when subject to dynamic loads and Fig. 19 b, the non-polarized sample response. Therefore, the sensitivity of the plate #4 increases from $5.1 \times 10^{-4} \mu\text{V}/\text{MPa}$ to $12.0 \times 10^{-4} \mu\text{V}/\text{MPa}$ when subjected to a polarization process and electrical signal becomes less noisy, which is possible to observe in Fig. 19 c.

5. Conclusion

This work allowed the possibility of granting a sensorial function to a metallic part avoiding several challenges in the integration of embedded sensors. The technological process used ensures the creation of a region that can be monitored because sensorial properties are introduced into the metal part turning it into a self-sensing material. This self-sensing material can be monitored in real-time and throughout its life cycle. In addition, the use of FSP improved the mechanical properties in the processed zone, not only by the process influence itself, but also by the incorporation of the BT ceramic particles.

It was demonstrated that the self-sensing material can present a sensitivity up to $12.0 \times 10^{-4} \mu\text{V}/\text{MPa}$ when subject to external dynamic loads. The use of particles with high piezoelectric properties and the polarization process are essential steps for the success of this innovation. The results presented are very promising, however it is important to optimize the methodologies and these processes to obtain better monitoring sensitivities, such as, use piezoelectric particles with higher piezoelectric properties, expand the range of the metal applications and use other technological processes to embedded particles inside the metallic components. In addition, the authors envisage that this self-sensing material may be used to temperature measurements or crack detection.

CRedit authorship contribution statement

Pedro M. Ferreira: Conceptualization, Methodology, Formal analysis, Investigation, Data curation, Writing – original draft, Visualization. **Miguel A. Machado:** Conceptualization, Methodology, Formal analysis, Writing – review & editing. **Marta S. Carvalho:** Conceptualization, Methodology, Formal analysis, Writing – review & editing. **Catarina Vidal:** Conceptualization, Methodology, Formal analysis, Resources, Writing – review & editing, Supervision, Project administration, Funding acquisition.

Declaration of Competing Interest

The authors declare that they have no known competing financial interests or personal relationships that could have appeared to influence the work reported in this paper.

Data availability

No data was used for the research described in the article.

Acknowledgements

The authors acknowledge Fundação para a Ciência e a Tecnologia (FCT-MCTES) for its financial support via the project UIDB/00667/2020 (UNIDEMI). PMF also acknowledges FCT-MCTES for funding the PhD grant UI/BD/151055/2021. The authors would like also to thank to Micronsense-Metrologia Industrial (Leiria, Portugal) for the μCT analysis. The authors would also like to thank Prof. Catarina Santos for granting access to the MicroLab - Electron Microscopy Laboratory (Instituto Superior Técnico) for the SEM analyses.

References

- [1] T.L. Anderson, T.L. Anderson, *Fracture Mechanics*, CRC Press, 2005. Doi: <https://doi.org/10.1201/9781420058215>.

- [2] D. Balageas, C.-P. Fritzen, A. Güemes, *Structural health monitoring*, vol. 90, John Wiley & Sons, 2010.
- [3] P.M. Ferreira, M.A. Machado, M.S. Carvalho, C. Vidal, *Embedded Sensors for Structural Health Monitoring: Methodologies and Applications Review*, *Sensors* 22 (2022) 8320, <https://doi.org/10.3390/s22218320>.
- [4] B.F. Spencer, M.E. Ruiz-Sandoval, N. Kurata, *Smart sensing technology: opportunities and challenges*, *Struct. Control. Heal. Monit* 11 (2004) 349–368, <https://doi.org/10.1002/stc.48>.
- [5] E. Oromiehie, B.G. Prusty, P. Compston, G. Rajan, *Characterization of process-induced defects in automated fiber placement manufacturing of composites using fiber Bragg grating sensors*, *Struct. Heal. Monit* 17 (2018) 108–117, <https://doi.org/10.1177/1475921716685935>.
- [6] K. Ksc, R. Kenny, M.P. Whelan, W.J. Cantwell, P.R. Chalker, *Embedded fibre Bragg grating sensors in advanced composite materials*, *Compos. Sci. Technol* 61 (2001) 1379–1387, [https://doi.org/10.1016/S0266-3538\(01\)00037-9](https://doi.org/10.1016/S0266-3538(01)00037-9).
- [7] R. Ramly, W. Kuntjoro, M.K.A. Rahman, *Using Embedded Fiber Bragg Grating (FBG) Sensors in Smart Aircraft Structure Materials*, *Procedia. Eng* 41 (2012) 600–606, <https://doi.org/10.1016/j.proeng.2012.07.218>.
- [8] F. Wu, F.-K. Chang, *Debond Detection using Embedded Piezoelectric Elements in Reinforced Concrete Structures - Part I: Experiment*, *Struct. Heal. Monit* 5 (2006) 5–15, <https://doi.org/10.1177/1475921706057978>.
- [9] H.-Y. Tang, C. Winkelmann, W. Lestari, V. La Saponara, *Composite structural health monitoring through use of embedded PZT sensors*, *J. Intell. Mater. Syst. Struct* 22 (2011) 739–755, <https://doi.org/10.1177/1045389X11406303>.
- [10] V. Talakkokula, S. Bhalla, *Reinforcement corrosion assessment capability of surface bonded and embedded piezo sensors for reinforced concrete structures*, *J. Intell. Mater. Syst. Struct* 26 (2015) 2304–2313, <https://doi.org/10.1177/1045389X14554133>.
- [11] A.K. Ramanathan, M.B. Gingerich, L.M. Headings, M.J. Dapino, *Metal structures embedded with piezoelectric PVDF sensors using ultrasonic additive manufacturing*, *Manuf. Lett* (2021), <https://doi.org/10.1016/j.mfglet.2021.08.001>.
- [12] M.S. Hossain, J.A. Gonzalez, R.M. Hernandez, M.A.I. Shuvo, J. Mireles, A. Choudhuri, et al., *Fabrication of smart parts using powder bed fusion additive manufacturing technology*, *Addit. Manuf* 10 (2016) 58–66, <https://doi.org/10.1016/j.addma.2016.01.001>.
- [13] C. Carradero Santiago, C. Randall-Posey, A.-A. Popa, L. Duggen, B. Vuksanovich, P. Cortes, et al., *3D Printed Elastomeric Lattices With Embedded Deformation Sensing*, *IEEE. Access* 8 (2020) 41394–41402, <https://doi.org/10.1109/ACCESS.2020.2973664>.
- [14] P. Stoll, E. Gasparin, A. Spierings, K. Wegener, *Embedding eddy current sensors into LPBF components for structural health monitoring*, *Prog. Addit. Manuf* 6 (2021) 445–453, <https://doi.org/10.1007/s40964-021-00204-3>.
- [15] V.R. Duarte, T.A. Rodrigues, M.A. Machado, J.P.M. Pragana, P. Pombinha, L. Coutinho, et al., *Benchmarking of Nondestructive Testing for Additive Manufacturing*, *3D Print Addit Manuf* 2021;8:263–70. Doi: <https://doi.org/10.1089/3dp.2020.0204>.
- [16] M.A. Machado, L.F.S.G. Rosado, N.A.M. Mendes, R.M.M. Miranda, T.J.G. dos Santos, *New directions for inline inspection of automobile laser welds using non-destructive testing*, *Int. J. Adv. Manuf. Technol* 118 (2022) 1183–1195, <https://doi.org/10.1007/s00170-021-08007-0>.
- [17] M.A. Machado, L.S. Rosado, N.M. Mendes, R.M. Miranda, T.G. Santos, *Multisensor Inspection of Laser-Brazed Joints in the Automotive Industry*, *Sensors* 21 (2021) 7335, <https://doi.org/10.3390/s21217335>.
- [18] F. Pinto, F. Ciampa, M. Meo, U. Polimeno, *Multifunctional SMARt composite material for in situ NDT/SHM and de-icing*, *Smart. Mater. Struct* 21 (2012), 105010, <https://doi.org/10.1088/0964-1726/21/10/105010>.
- [19] X. Li, A. Golnas, F.B. Prinz, *Shape deposition manufacturing of smart metallic structures with embedded sensors*, in: Claus RO, Spillman, Jr. WB, editors. *Smart Struct. Mater. 2000 Sens. Phenom. Meas. Instrum. Smart Struct. Mater.*, vol. 3986, 2000, p. 160. Doi: <https://doi.org/10.1117/12.388103>.
- [20] X.C. Li, F. Prinz, J. Seim, *Thermal behavior of a metal embedded fiber Bragg grating sensor*, *Smart. Mater. Struct* 10 (2001) 575–579, <https://doi.org/10.1088/0964-1726/10/4/301>.
- [21] X. Li, F. Prinz, *Metal Embedded Fiber Bragg Grating Sensors in Layered Manufacturing*, *J. Manuf. Sci. Eng* 125 (2003) 577–585, <https://doi.org/10.1115/1.1581889>.
- [22] X. Li, F. Prinz, *Analytical and Experimental Study on Noncontact Sensing With Embedded Fiber-Optic Sensors in Rotating Metal Parts*, *J. Light. Technol* 22 (2004) 1720–1727, <https://doi.org/10.1109/JLT.2004.829231>.
- [23] X. Zhang, H. Jiang, L.X. Design, *Fabrication, and Characterization of Metal Embedded Microphotonic Sensors*, *J. Manuf. Sci. Eng* (2008) 130, <https://doi.org/10.1115/1.2917356>.
- [24] J.J. Schomer, M.J. Dapino, *High Temperature Characterization of Fiber Bragg Grating Sensors Embedded Into Metallic Structures Through Ultrasonic Additive Manufacturing*. Vol. 2 Model. Simul. Control Adapt. Syst. Integr. Syst. Des. Implementation; *Struct. Heal. Monit.*, vol. 58264, American Society of Mechanical Engineers; 2017, p. V002T05A003. Doi: <https://doi.org/10.1115/SMASIS2017-3840>.
- [25] S.K. Chilelli, J.J. Schomer, M.J. Dapino, *Detection of Crack Initiation and Growth Using Fiber Bragg Grating Sensors Embedded into Metal Structures through Ultrasonic Additive Manufacturing*, *Sensors* 19 (2019) 4917, <https://doi.org/10.3390/s19224917>.
- [26] A. Hehr, M. Norfolk, D. Kominsky, A. Boulanger, M. Davis, P. Boulware, *Smart Build-Plate for Metal Additive Manufacturing Processes*, *Sensors* 20 (2020) 360, <https://doi.org/10.3390/s20020360>.

- [27] X. Cheng, A. Datta, H. Choi, X. Zhang, X. Li, Study on Embedding and Integration of Microsensors Into Metal Structures for Manufacturing Applications, *J. Manuf. Sci. Eng* 129 (2007) 416–424, <https://doi.org/10.1115/1.2515456>.
- [28] R. Hahnlen, M.J. Dapino, Active metal-matrix composites with embedded smart materials by ultrasonic additive manufacturing, in: McMickell MB, Farinholt KM, editors. *Ind. Commer. Appl. Smart Struct. Technol.* 2010, vol. 7645, 2010, p. 764500. Doi: <https://doi.org/10.1117/12.848853>.
- [29] M. Juhász, R. Tiedemann, G. Dumstorf, J. Walker, P.A. Du, B. Conner, et al., Hybrid directed energy deposition for fabricating metal structures with embedded sensors, *Addit. Manuf* 35 (2020), 101397, <https://doi.org/10.1016/j.addma.2020.101397>.
- [30] Z.Y. Ma, Friction Stir Processing Technology: A Review, *Metall. Mater. Trans. A* 39 (2008) 642–658, <https://doi.org/10.1007/s11661-007-9459-0>.
- [31] A. Kurt, I. Uygur, E. Cete, Surface modification of aluminium by friction stir processing, *J. Mater. Process. Technol* 211 (2011) 313–317, <https://doi.org/10.1016/j.jmatprotec.2010.09.020>.
- [32] Y. Gan, D. Solomon, M. Reinbolt, Friction Stir Processing of Particle Reinforced Composite Materials, *Materials. (Basel)* 3 (2010) 329–350, <https://doi.org/10.3390/ma3010329>.
- [33] C. Vidal, P. Alves, M.M. Alves, M.J. Carmezim, M.H. Fernandes, L. Grenho, et al., Fabrication of a biodegradable and cytocompatible magnesium/nanohydroxyapatite/fluorapatite composite by upward friction stir processing for biomedical applications, *J. Mech. Behav. Biomed. Mater* 129 (2022), 105137, <https://doi.org/10.1016/j.jmbbm.2022.105137>.
- [34] P. Vilaca, J. Gandra, C. Vidal, Linear Friction Based Processing Technologies for Aluminum Alloys: Surfacing, Stir Welding and Stir Channeling, *Alum. Alloy. - New. Trends. Fabr. Appl., InTech* (2012), <https://doi.org/10.5772/52026>.
- [35] P.A. Bajakke, V.R. Malik, A.S. Deshpande, Particulate metal matrix composites and their fabrication via friction stir processing – a review, *Mater. Manuf. Process* 34 (2019) 833–881, <https://doi.org/10.1080/10426914.2019.1605181>.
- [36] M. Akbari, P. Asadi, H.R. Asiabaraki, Investigation of wear and microstructural properties of A356/ TiC composites fabricated by FSP, *Surf. Rev. Lett* 29 (2022) 1–10, <https://doi.org/10.1142/S0218625X2250130X>.
- [37] M. Akbari, P. Asadi, Simulation and experimental investigation of multi-walled carbon nanotubes/aluminum composite fabrication using friction stir processing, *Proc. Inst. Mech. Eng. Part. E. J. Process. Mech. Eng* 235 (2021) 2165–2179, <https://doi.org/10.1177/09544089211034029>.
- [38] H. Lu, X. Wang, T. Zhang, Z. Cheng, Q. Fang, Design, Fabrication, and Properties of High Damping Metal Matrix Composites—A Review, *Materials. (Basel)* 2 (2009) 958–977, <https://doi.org/10.3390/ma2030958>.
- [39] V. Sharma, U. Prakash, B.V.M. Kumar, Surface composites by friction stir processing: A review, *J. Mater. Process. Technol* 224 (2015) 117–134, <https://doi.org/10.1016/j.jmatprotec.2015.04.019>.
- [40] P.L. Inácio, F. Nogueira, F.B. Ferreira, C. Vidal, N. Schell, T. Tero, et al., Functionalized material production via multi-stack Upward Friction Stir Processing (UFSP), *Mater. Manuf. Process* 37 (2022) 11–24, <https://doi.org/10.1080/10426914.2021.1942909>.
- [41] T.G. Santos, J.P. Oliveira, M.A. Machado, P.L. Inácio, V.R. Duarte, T.A. Rodrigues, et al. *Reliability and NDT Methods. Adv. Struct. Mater.*, vol. 129, Springer; 2020, p. 265–95. Doi: https://doi.org/10.1007/978-3-030-44522-5_8.
- [42] J.A. Gallego-Juarez, Piezoelectric ceramics and ultrasonic transducers, *J. Phys. E* 22 (1989) 804–816, <https://doi.org/10.1088/0022-3735/22/10/001>.
- [43] W.G. Cady, *Piezoelectricity: Volume Two: An Introduction to the Theory and Applications of Electromechanical Phenomena in Crystals.* Courier Dover Publications, 2018.
- [44] S. Thapliyal, D.K. Dwivedi, Barium titanate reinforced nickel aluminium bronze surface composite by friction stir processing, *Mater. Sci. Technol. (United Kingdom)* 34 (2018) 366–377, <https://doi.org/10.1080/02670836.2017.1393203>.
- [45] C. Vidal, V. Infante, P. Vilaça, Metallographic and morphological characterization of sub-surface friction stirred channels produced on AA5083-H111, *Int. J. Adv. Manuf. Technol* 105 (2019) 2215–2235, <https://doi.org/10.1007/s00170-019-04459-7>.
- [46] X. Xi, D.D.L. Chung, Piezoresistivity and piezoelectricity discovered in aluminum, with relevance to structural self-sensing, *Sensors. Actuators. A. Phys* 289 (2019) 144–156, <https://doi.org/10.1016/j.sna.2019.02.013>.
- [47] C. Vidal, V. Infante, P. Vilaça, Characterisation of fatigue fracture surfaces of friction stir channelling specimens tested at different temperatures, *Eng. Fail. Anal* 56 (2015) 204–215, <https://doi.org/10.1016/j.engfailanal.2015.02.009>.
- [48] J.F. Tressler, S. Alkoy, R.E. Newnham, Piezoelectric sensors and sensor materials, *J. Electroceramics* 2 (1998) 257–272, <https://doi.org/10.1023/A:1009926623551>.
- [49] G. Arlt, D. Hennings, G. De With, Dielectric properties of fine-grained barium titanate ceramics, *J. Appl. Phys* 58 (1985) 1619–1625, <https://doi.org/10.1063/1.336051>.
- [50] T. Hoshina, K. Takizawa, J. Li, T. Kasama, H. Kakemoto, T. Tsurumi, Domain size effect on dielectric properties of barium titanate ceramics, *Jpn. J. Appl. Phys* 47 (2008) 7607–7611, <https://doi.org/10.1143/JJAP.47.7607>.
- [51] L. Wu, M.-C. Chure, K.-K. Wu, W.-C. Chang, M.-J. Yang, W.-K. Liu, et al., Dielectric properties of barium titanate ceramics with different materials powder size, *Ceram. Int* 35 (2009) 957–960, <https://doi.org/10.1016/j.ceramint.2008.04.030>.
- [52] G.L. Sorger, J.P. Oliveira, P.L. Inácio, N. Enzinger, P. Vilaça, R.M. Miranda, et al., Non-destructive microstructural analysis by electrical conductivity: Comparison with hardness measurements in different materials, *J. Mater. Sci. Technol* 35 (2019) 360–368, <https://doi.org/10.1016/j.jmst.2018.09.047>.
- [53] T.G. Santos, R.M. Miranda, P. Vilaça, J.P. Teixeira, J. dos Santos, Microstructural mapping of friction stir welded AA 7075-T6 and AlMgSc alloys using electrical conductivity, *Sci. Technol. Weld. Join* 16 (2011) 630–635, <https://doi.org/10.1179/1362171811Y.0000000052>.
- [54] T. Santos, P. Vilaça, L. Quintino, Developments in NDT for detecting imperfections in friction stir welds in aluminium alloys, *Weld. World* 52 (2008) 30–37, <https://doi.org/10.1007/BF03266666>.
- [55] M.A. Machado, L.S. Rosado, T.G. Santos, Shaping Eddy Currents for Non-Destructive Testing Using Additive Manufactured Magnetic Substrates, *J. Nondestruct. Eval* 41 (2022) 1–11, <https://doi.org/10.1007/s10921-022-00882-1>.